SOFT ROBOTICS
Volume 6, Number 1, 2019
© Mary Ann Liebert, Inc.
DOI: 10.1089/soro.2018.0037

ORIGINAL ARTICLE

Dielectric Elastomer Spring-Roll Bending Actuators: Applications in Soft Robotics and Design

Jinrong Li,[1] Liwu Liu,[2] Yanju Liu,[2] and Jinsong Leng[1]

Abstract

Soft robotics is an emerging area that attracts more and more attention. The intrinsic flexibility and compliance of soft materials and structures would endow novel functions with soft robots. Dielectric elastomers could deform sustainably subjected to external electrical stimuli and become promising materials for soft robots due to the large actuation strain, low elastic modulus, fast response, and high energy density. This article focuses on the fabrication, applications, and design of the dielectric elastomer spring-roll bending actuators. The actuator with large electrically induced bending angle has been made and demonstrated the applications in flexible gripper and inchworm-inspired soft crawling robot. The basic performance of the gripper and the crawling robot has been characterized. Furthermore, a thermodynamic model has been established to investigate the deformation and failure of such actuators. Comparison between theoretical and test results shows that the model is suitable for the prediction of the performance of the actuator. Then the influence of some design parameters on the performance of the actuator has been analyzed and discussed based on the model. The results could provide guidance to the design and optimization of such actuators for different applications.

Keywords: dielectric elastomer, soft robots, thermodynamic model, actuator design

Introduction

Soft robotics is an emerging area inspired by soft animals in nature, and the development of soft robots highly relies on the advances of soft materials or flexible structures.[1–3] Variable soft robots have been designed and fabricated based on pneumatic actuation,[4–9] shape memory materials[10–14] electroactive polymers,[15–22] liquid metals,[23] and so on. Compared with traditional robots built with hard material, soft robots have the advantages of lighter weight, larger continuum deformation, and better adaptivity to complex environments. The intrinsic flexibility and compliance of soft materials not only simplify or minimize the robot structures but also make the soft robots possess some special features that are hard to be realized in traditional robots, such as self-healing,[24] growth,[9,25] and movements through gaps or constrained environment.[5,9]

Dielectric elastomers are typical electroactive polymers that can response to external electrical stimuli. Normally, it is a sandwiched structure composed of one elastomer film layer and compliant electrodes on two opposite surfaces.[26] Subjected to external electric field, a dielectric elastomer would reduce its thickness and enlarge its area due to Maxwell stress. The large actuation strain, fast response, and high-energy density make dielectric elastomer a promising material for soft robots.[27] Various types of actuators have been fabricated based on dielectric elastomers and have demonstrated applications in walking robots,[15–17] wrestling robots,[28] facial expression,[29] tunable lens,[30] grippers,[18,19,31] airship,[32] active hinges,[33] and so on.

In this article, we focus on the fabrication, applications, and design of dielectric elastomer spring-roll bending actuator. Slightly different from the spring-roll actuators with multiple degrees-of-freedom,[15] only the film parts in onside of our bending actuator are active to achieve a larger bending angle with the sacrifice of the multiple degrees-of-freedom movement, since the circumferential angle of the coated compliant electrodes could be larger than π. It may also reduce the complexity in fabrication and control for some applications where one directional bending is required. The flexible gripper and inchworm-inspired crawling robot have been fabricated based on such actuators as possible

[1]Center for Composite Materials and Structures, Harbin Institute of Technology, Harbin, China.
[2]Department of Astronautical Science and Mechanics, Harbin Institute of Technology, Harbin, China.

applications in soft robotics and their basic performance has been characterized. Furthermore, a thermodynamic model has also been established to theoretically investigate the deformation and failure of the spring-roll bending actuator. On the basis of this model, the influences of some design parameters on the actuator performance have been analyzed and discussed. That will provide the guidance for the design and optimization of the dielectric elastomer spring-roll actuator for different practical applications.

Dielectric Elastomer Spring-Roll Bending Actuator and Its Applications in Soft Robotics

Fabrication and performance of the spring-roll bending actuators

The dielectric elastomer spring-roll actuator is composed of a compressed spring as the core, a stretched dielectric elastomer film (VHB 4910 produced by 3M Company) wrapping around the spring, carbon grease (produced by MG Chemicals) as compliant electrodes coated only on the film parts at one side of the actuator, and two caps to prevent the spring from slipping or protruding due to the restoring force and viscosity of VHB tape.

The fabrication process of the spring-roll bending actuator is illustrated in Figure 1 and described as follows. (1) The spring is precompressed using the caps and supporting structure, which will be taken out after the fabrication. The precompression of spring could maintain a higher longitudinal prestretch ratio of the VHB film. (2) The VHB film is biaxial prestretched and only the central part of film that has more uniform prestretch will be used. (3) The carbon grease was coated on the prestretched film using a mask to form rectangular electrodes with calculated distances to ensure that the electrodes could stack at one side of the actuator. Each electrode is connected to a copper wire for applying high voltage. The wires connected to adjacent electrodes have opposite directions and are connected to the high voltage and ground, respectively. The number of electrodes could be altered based on different requirements or design. (4) The precompressed spring (with the supporting structure) is rolled over the coated VHB film to let the film wrap around the spring and finally the supporting structure is taken out.

The resulted spring-roll bending actuator and its performance are shown in Figure 2 and Supplementary Video S1. In Supplementary Video S1, the actuator acted in the form of a cantilever beam with one end fixed by the clamp and the applied voltage rose from 2 to 6 kV. The actuator failed when the applied voltage is 6 kV.

Flexible gripper

Based on the electrically induced bending deformation of this kind of actuator, some applications in soft robotics have been explored. With the help of 3D printing technology, we have designed and fabricated a three-finger flexible gripper that is composed of 3D-printed structures and three spring-roll bending actuators. Each actuator has an effective length of about 5 mm and weight of around 11 g. The actuators are electrically connected in parallel and the control wires are tethered to the gripper and hide inside the 3D-printed structures to prevent danger of high voltage to human body. The rest and grasping states of the gripper are demonstrated in Figure 3. Supplementary Video S2 shows the gripper grasped an object and released it into a box incorporated with a remotely controlled toy crane truck.

To evaluate the performance of the flexible gripper, the maximum pull-out force under different input voltages was tested. The gripper first grasped a container and then the water was added drop by drop until the container fell from the gripper (Supplementary Video S3). The pull-out force was calculated from the maximum gross weight of the container and water. It should be noted that the pull-out force is determined by the shape and size of the grasped object and also the adhesion or friction between the object and gripper.

In this study, the container we used is cut from a bottle and its maximum radius is close to that of the inner circle of the gripper. Also, each end of the actuator was wrapped by heat shrink tubing with smooth surface to avoid adhesion between the VHB tape and container since that adhesion may generate uncertainty of results. The measured pull-out force was 171.5, 193.7, and 228.3 mN when the applied voltage is 4, 4.5, and 5 kV, respectively. The pull-out force would rise if sticky or rough surface was put on the end of each actuator to provide higher friction. The gripper should have higher pull-out force under higher applied voltage. In fact, it could grasp the container at a higher voltage such as 5.5 kV. However, one of the actuators would fail before we obtain a reliable result when that voltage is applied for quite a long time.

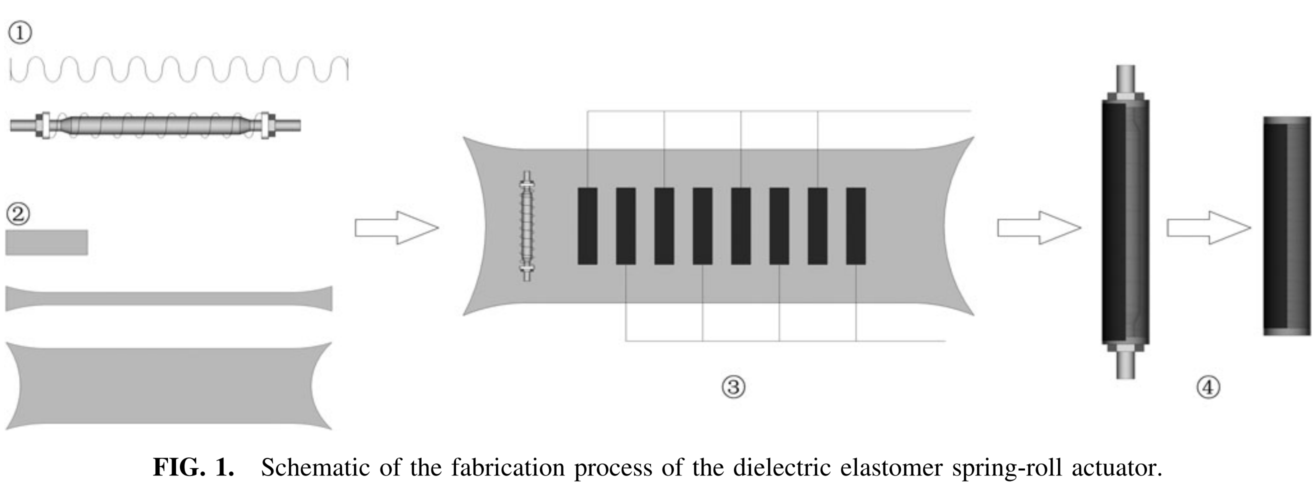

FIG. 1. Schematic of the fabrication process of the dielectric elastomer spring-roll actuator.

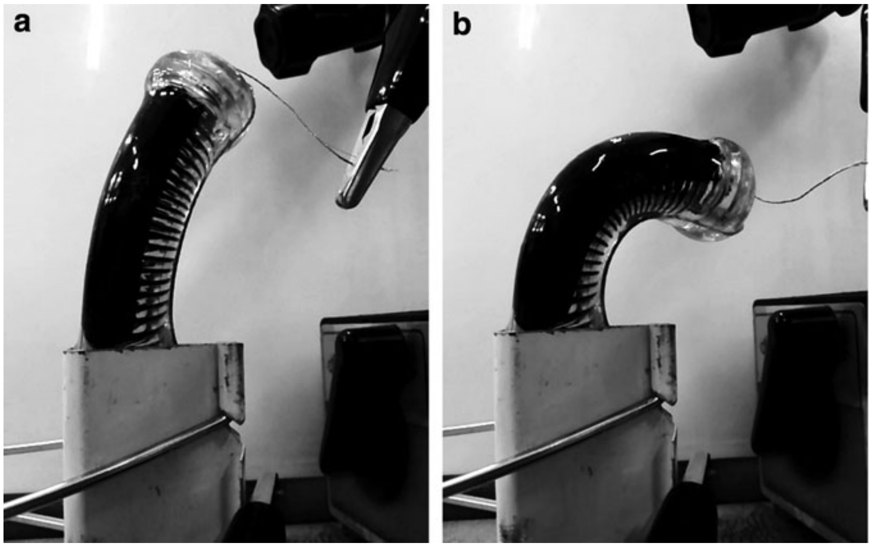

FIG. 2. The shape of the spring-roll bending actuator when **(a)** no voltage is applied and **(b)** the applied voltage is 6 kV.

Inchworm-inspired crawling robots

The bending and unbending of the spring-roll actuator are similar to the deformation of some mollusks. So here we also demonstrate an inchworm-inspired crawling robot based on this kind of actuator. The structure of this crawling robot is quite simple and consists of a spring-roll actuator and two end caps (Fig. 4). There are two bundles of oriented plastic fibers at the bottom of each end cap to provide anisotropic friction so that the robot could move forward on surfaces that is not too smooth, such as paper, when a sinusoidal high voltage is applied. The spring used in this crawling robot is longer than that used in the flexible gripper since the buckling of the spring could make the actuator curved so that it is easier to realize the anisotropic friction.

The applied voltage is generated from a functional waveform generator and amplified (1000 times) by a high-voltage amplifier (Trek Model 10/40A). The actuator should have larger deformation at lower input voltage frequency in principle. However, the gravity force and friction force between the oriented fibers and bottom surface would reduce the deformation of the actuator. Thus, the speed of the crawling robot at low frequency of input voltage is lower than that at higher frequency. On the contrary, when the input voltage frequency is too high, the crawling robot will oscillate severely with random moving direction rather than crawling forward. The suitable frequency interval would be 10–20 Hz from our test (Supplementary Videos S4 and S5). The tested crawling speed of the robot is 15, 22.5, and 26.3 mm/s, respectively, when the applied voltage has amplitude of 0–6 kV and frequency of 10, 15, and 20 Hz.

Model of the Actuator

Model establishment

For better understanding and optimization of the spring-roll actuator, the following part of this article focuses on the

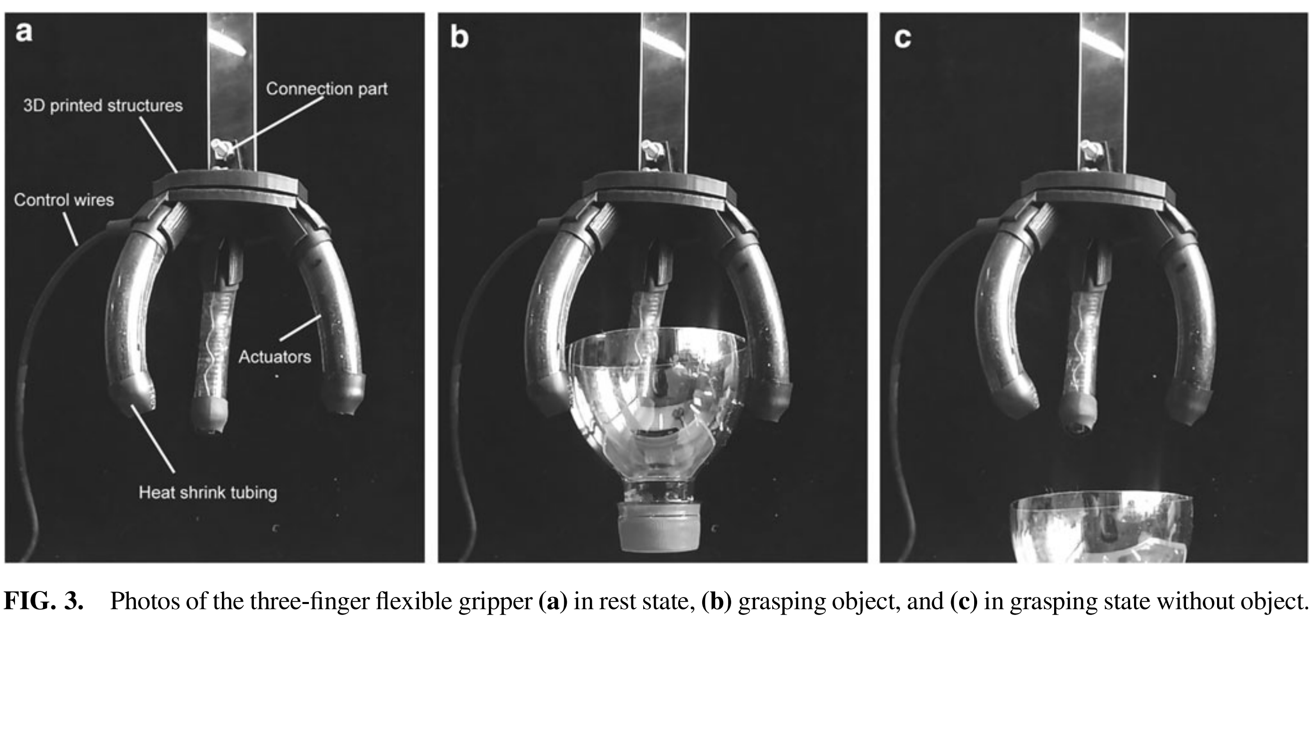

FIG. 3. Photos of the three-finger flexible gripper **(a)** in rest state, **(b)** grasping object, and **(c)** in grasping state without object.

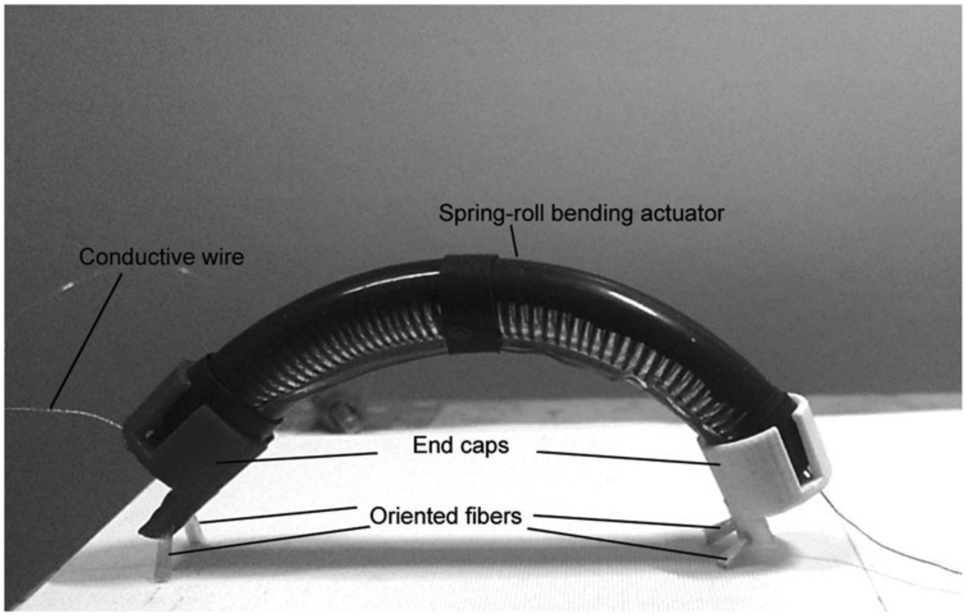

FIG. 4. Photo of the inchworm-inspired crawling robot.

modeling and design of this kind of actuator. The actuator is regarded as a thermodynamic system that consists of compressed spring and multilayer stretched film. The compliant electrodes are assumed to have no stiffness and only determine which layer is active. Actually, all layers at the active side of the actuator besides the innermost and outermost layers are active since both surfaces of such layers are coated with carbon grease. First, we illustrate the definitions of some parameters in the actuator. The circumferential angles of both the active area and inactive area are assumed to be equal to π, representing an ideal state. Although from the same film, the active and inactive areas are regarded as two separate parts since the dielectric energy of only the active area will be considered. Figure 5a shows the dimension changes of the spring and innermost layer during the fabrication process.

The cross section of the spring used is circle and the free length, outside radius, and wire diameter of the spring are denoted by L_0, r, and d, respectively. The precompression ratio λ_s represents the ratio of the length of spring after precompression over its initial length. The VHB films in the active and inactive area have stretch ratios in two directions of λ_1, λ_2, and λ_1', λ_2', respectively, and the innermost layer of the actuator has a dimension of $L_1 \times L_2 \times L_3$ at reference state. In the prestretch state, we have $\lambda_1 = \lambda_1' = \lambda_{1p}$ and $\lambda_2 = \lambda_2' = \lambda_{2p}$. From the geometrical relationships, we can obtain that

$$\lambda_{1p} L_1 = \lambda_s L_0, \tag{1}$$

$$\lambda_{2p} L_2 = \pi r. \tag{2}$$

As described before, there are totally $N+2$ layers in an actuator with N active layers. We number each layer from 0 to $N+1$ as shown in Figure 5b. The thickness of the prestretched film is $L_3 / \lambda_{1p}\lambda_{2p}$, in which L_3 is also the thickness of VHB tape and is denoted by d_0. Then for the n-th layers, the circumferential geometrical relationship becomes

$$\lambda_{2p} L_{2(n)} = \pi\left(r + \frac{nd_0}{\lambda_{1p}\lambda_{2p}}\right), \tag{3}$$

or

$$L_{2(n)} = L_2\left(1 + \frac{nd_0}{r\lambda_{1p}\lambda_{2p}}\right), \tag{4}$$

where the terms in the bracket could not be neglected especially when n is large since d_0 and r are in the same order.

Then we analyze the deformation of the actuator under external load. The parameters defined so far are corresponding to the state that the supporting structure is not taken out when fabrication. After the supporting structure is taken out, the system will reach a new equilibrium. The deformation in this process is called initial deformation in this article. The initial deformation will determine the final length of the actuator. In most cases, the actuator will further elongate or contract in this process and the longitudinal stretch ratios of the film on both sides are uniform. In the final state after initial deformation, we would have $\lambda_1 = \lambda_1' = \lambda_{1i}$.

The circumferential stretch of the film is restrained by the spring and the adhesion between inactive layers. The circumferential deformation of the outmost active layer is not too large as can be seen from Supplementary Video S1. So the dielectric elastomer film is assumed to be in pure shear state[34] for simplification. Then the equation $\lambda_2 = \lambda_2' = \lambda_{2p}$ holds in both initial deformation and bending deformation. When the external voltage is applied, the active layers will expand in longitudinal direction so that the actuator will bend. The longitudinal stretches will be determined by the angular position and also the bending angle of the actuator. That will result in implicit equations. To avoid complexity in solving implicit equations, here we take the assumption that the longitudinal stretch is uniform in each layer, which is similar to the stroke assumption mentioned in Pei *et al.*[15] Although inducing inaccuracies in results, such simplification is still valid in investigating the influences of design parameters on the performance of the actuator.

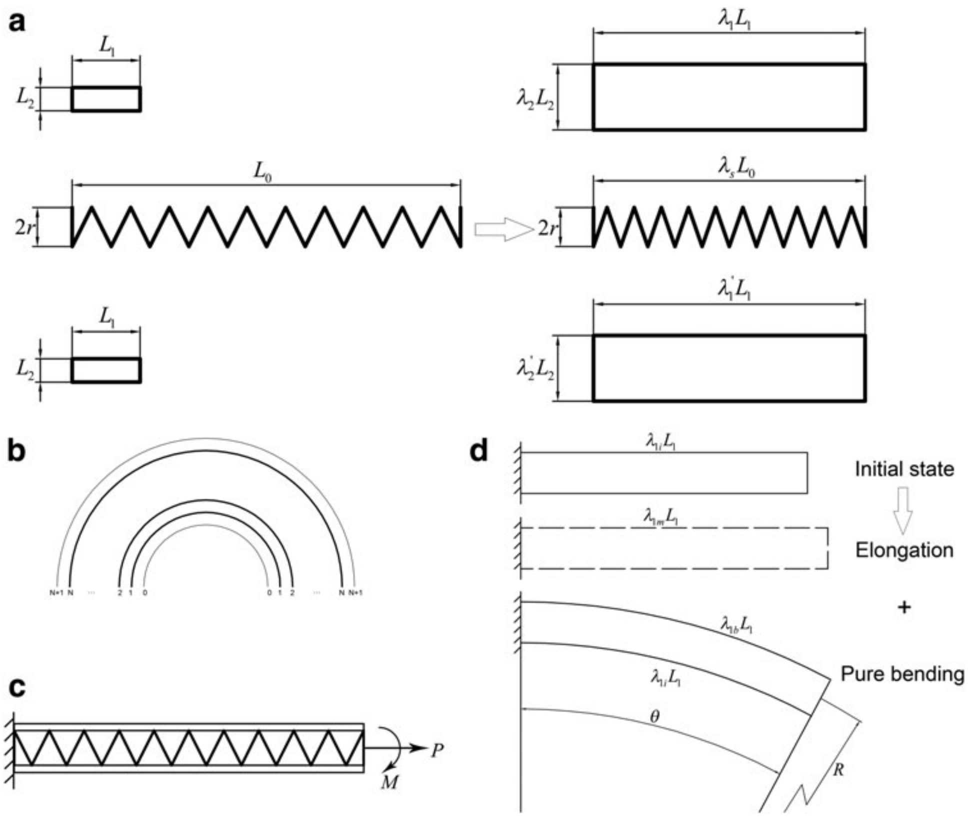

FIG. 5. **(a)** Dimension changes of the dielectric elastomer film after prestretch and the spring after precompression; **(b)** schematic of the number of each layer in which the thick lines represent the active layers that were coated with electrodes on both sides and the fine lines represent the inactive layers; **(c)** equivalent loading state of the actuator when the external voltage is applied; **(d)** illustration of the superposition of the bending actuation of the actuator and geometric parameter change in this process.

During the bending deformation, for the spring, the equivalent mechanical load is an axial tensile force P and a bending moment M in this condition, as shown in Figure 5c. Thus, the final deformation of the actuator is the superposition of elongation and pure bending. Based on the above discussion, the bending process of the actuator is described as follows concerning the stretch ratio changes of the innermost layers, and illustrated in Figure 5d. The longitudinal stretch ratios of the active and inactive parts change from λ_{1i} to λ_{1m} first and then become λ_{1b} and $\lambda_{1b}^{'}$, respectively, when the bending angle is θ. In Supplementary Video S1, the pitch of the compressed spring in the inactive part, which is transparent, has no obvious change when it bends. Then we have $\lambda_{1b}^{'} = \lambda_{1i}$ and the geometrical relationship of λ_{1m}, λ_{1b}, $\lambda_{1b}^{'}$, and θ becomes

$$\lambda_{1m} = \frac{\lambda_{1b} + \lambda_{1b}^{'}}{2}, \tag{5}$$

$$\theta = \frac{(\lambda_{1b} - \lambda_{1i})L_1}{2r}. \tag{6}$$

For the n-th layer, the longitudinal stretch ratio is written as follows:

$$\lambda_{1(n)} = \lambda_1 (1 + \frac{nd_0}{(R+r)\lambda_{1p}\lambda_{2p}}), \tag{7}$$

where R is the curvature radius of the actuator. The calculation results show that R is more than 50 times of d_0 even when the bending angle is more than 90°. So we can just take $\lambda_{1(n)} = \lambda_1$ for approximation when n is less than 20 (this value could be larger if VHB4905 is used).

The ideal dielectric elastomer model, which has been used almost exclusively to analyze the dielectric elastomers and their actuators,[35–38] is utilized as the material model and the incompressible neo-Hookean model is used to describe the nonlinear mechanical behavior of the VHB. The spring is assumed to be linearly elastic since the force/displacement curve of the spring remains linear even when the spring is compressed by 50%.

Then we can formulate the Helmholtz free energy of the whole system. It is the function of two generalized coordinates, the longitudinal stretch of the innermost layer in the active part λ_1 and the charge Q in one electrode of the first active layer. $\lambda_1^{'}$ will also appear in the expression of the Helmholtz free energy, but it is not independent based on the aforementioned discussion and thus could not be regarded as the generalized coordinate. All the active layers could be regarded as compliant capacitors that connected in parallel and have the same dielectric energy density. If the positive charge on the first active layer is Q, the positive charge on the n-th layer would be $QL_{2(n)}/L_2$. Then the dielectric energy of the n-th layer is

$$E_{\varepsilon(n)} = \frac{1}{2\varepsilon}\left(\frac{Q}{\lambda_1 L_1 \lambda_{2p} L_2}\right)^2 L_1 L_{2(n)} L_3. \tag{8}$$

Thus, the Helmholtz free energy of the whole system is written as follows:

$$\mathrm{H}(\lambda_1, Q) = \frac{\mu}{2}\left(\lambda_1^2 + \lambda_{2p}^2 + \lambda_1^{-2}\lambda_{2p}^{-2} - 3\right)L_1L_2L_3\sum_{n=0}^{N+1}\left(1 + \frac{nd_0}{r\lambda_{1p}\lambda_{2p}}\right) + \frac{1}{2\varepsilon}\left(\frac{Q}{\lambda_1 L_1 \lambda_{2p} L_2}\right)^2\sum_{n=1}^{N}\left(1 + \frac{nd_0}{r\lambda_{1p}\lambda_{2p}}\right)$$
$$+ \frac{\mu}{2}\left(\lambda_1'^2 + \lambda_{2p}^2 + \lambda_1'^{-2}\lambda_{2p}^{-2} - 3\right)L_1L_2L_3\sum_{n=0}^{N+1}\left(1 + \frac{nd_0}{r\lambda_{1p}\lambda_{2p}}\right) + E_s, \tag{9}$$

where E_s is the elastic energy stored in the spring. Consider that the system is in equilibrium under axial tensile force P, external bending moment M, and applied voltage Φ. The change of free energy is attributed to the work done by mechanical load and electrical load. For any small change in deformation or charge, we have

$$dH = PL_1 d\lambda_1 + Md\theta + \sum_{n=1}^{N}\left(1 + \frac{nd_0}{r\lambda_{1p}\lambda_{2p}}\right)\Phi dQ. \tag{10}$$

From Equation (6), θ is the function of λ_1 and thus Equation (10) is rewritten as follows:

$$dH = \left(P + \frac{M}{2r}\right)L_1 d\lambda_1 + \sum_{n=1}^{N}\left(1 + \frac{nd_0}{r\lambda_{1p}\lambda_{2p}}\right)\Phi dQ. \tag{11}$$

Taking λ_1 and Q as the generalized coordinates, the generalized mechanical load and the generalized electrical load are the partial derivatives of free energy. That is,

$$P + \frac{M}{2r} = \frac{\partial H(\lambda_1, Q)}{L_1 \partial \lambda_1}, \tag{12}$$

and

$$\Phi = \frac{\partial H(\lambda_1, Q)}{\sum_{n=1}^{N}\left(1 + \frac{nd_0}{r\lambda_{1p}\lambda_{2p}}\right)\partial Q}, \tag{13}$$

where $(P + M/2r)$ and Φ are the generalized mechanical and electrical loads, respectively. Equations (12) and (13) are the state equations of the system and thus we can analyze the deformation of the actuator.

Initial deformation

Before calculating the deformation of the actuator, some material constants and design parameters of the actuator are listed in Table 1. These design parameters are the same as that of the actuator we used to measure the bending angle under different applied voltages (in the part of actuator design) and used in the following part of this section. In the initial deformation process, no mechanical or electrical load is applied. So we could have $\Phi = 0$ and $Q = 0$. The state of the actuator could be determined by Equation (12) only. Due to the assumption that the deformation of the spring is linear, the elastic energy of the spring is as follows:

$$E_s = \frac{k}{2}(L_0 - \lambda_{1i}L_i)^2, \tag{14}$$

where $k = Ed^4 \big/ [16n(1+\nu)(2r-d)^3]$ is the spring constant.[39] Then the free energy of the system becomes

$$H(\lambda_{1i}) = \mu\left(\lambda_1^2 + \lambda_{2p}^2 + \lambda_1^{-2}\lambda_{2p}^{-2} - 3\right)$$
$$L_1L_2L_3\sum_{n=0}^{N+1}\left(1 + \frac{nd_0}{r\lambda_{1p}\lambda_{2p}}\right) + \frac{k}{2}(L_0 - \lambda_{1i}L_i)^2, \tag{15}$$

and the state Equation (12) becomes

$$\left(\lambda_{1\mathrm{i}} - \lambda_{2p}^{-2}\lambda_{1i}^{-3}\right)\sum_{n=0}^{N+1}\left(1 + \frac{nd_0}{r\lambda_{1p}\lambda_{2p}}\right) + \alpha_k\left(\lambda_{1i} - \frac{\lambda_{1p}}{\lambda_s}\right) = 0, \tag{16}$$

where $\alpha_k = k\lambda_s\lambda_{2p}L_0 \big/ (2\mu\pi r d_0 \lambda_{1p})$ is a dimensionless parameter that is positively correlated to the ratio between the axial stiffness of the spring and that of the dielectric elastomer film and determined by the material properties and some design parameters. From Equation (16), we obtain the final stretch ratio λ_{1i} of the actuator and thus the actuator length $L_a = \lambda_{1i}L_1 = \lambda_{1i}\lambda_s L_0 / \lambda_{1p}$. Figure 6 shows the length of actuators with different spring precompression ratios and different active layer numbers. The dash line represents the

Table 1. Material Constants and Design Parameters of the Actuator

	Symbol	*Value*
Material constants		
Young's modulus of the spring steel	E	1.9 GPa
Poisson's ratio of the spring steel	ν	0.3
Shear modulus of the dielectric elastomer (fitted value from uniaxial tension testing data)	μ	36 kPa
Design parameters		
Longitudinal prestretch ratio (average measurement value)	λ_{1p}	2.5
Circumferential prestretch ratio (average measurement value)	λ_{2p}	2.75
Precompression ratio	λ_s	0.65
Thickness of the dielectric elastomer	d_0	1 mm (VHB 4910)
Free length of the spring	L_0	100 mm
Outside radius of the spring	r	10 mm
Spring wire diameter	d	0.9 mm
Helix angle of the spring in free state	α	6.8°
Coil number of the spring (dependent on the free length)	n	27
Number of active dielectric elastomer layers	N	10

length of the spring after precompression. The area above the dash line means that the spring will elongate to further stretch the film and, accordingly, the area below the dash line means that the spring will be further compressed due to the contraction of the film.

Bending deformation

Based on the previous analysis, the elastic energy stored in the spring when the actuator is subjected to external voltage is due to the contributions of two deformation processes, axial tension and pure bending. So we have

$$E_s = \frac{P\Delta L}{2} + \frac{M\Delta\theta}{2}. \tag{17}$$

Here we introduce the equivalent cantilever beam bending stiffness of the spring

$$B = \frac{Ed^4 L\cos\alpha}{32n(2r-d)\left[1+\sin^2\alpha+(1+\upsilon)\cos^2\alpha\right]} \tag{18}$$

that represents the bending moment required to be applied on the spring with unit length to induce a bending angle of 1 rad.[39] Then the bending angle of the spring under a bending moment M is $\theta = ML/B$. It should be note that L in Equation (18) is the length of the spring after axial tension, or $L = L_m$. Also, the helix angle α will be changed when the spring is compressed. From Table 1, when the spring is in its free length, α is small enough so that $\sin^2\alpha \approx 0$ and $\cos\alpha \approx 1$. Then the equivalent cantilever beam bending stiffness of the spring in free length is simplified as follows:

$$B_0 = \frac{Ed^4 L_0}{32n(2+\nu)(2r-d)}. \tag{19}$$

So we have $B_m = B_0 L_m / L_0 = B_0 \lambda_{1m}\lambda_s/\lambda_{1p}$. Then in bending deformation, we have

$$\begin{aligned} E_s &= \frac{k(\Delta L)^2}{2} + \frac{B_m(\Delta\theta)^2}{2L_m} \\ &= \frac{kL_0^2(\lambda_{1p}-\lambda_m\lambda_s)}{2\lambda_{1p}^2} + \frac{B_0 L_0 \lambda_s^2(\lambda_{1b}-\lambda_{1i})^2}{8r^2\lambda_{1p}^2}. \end{aligned} \tag{20}$$

For the case that no external mechanical load is applied, substituting Equations (20) and (9) into Equations (12) and (13) gives

$$\begin{aligned} \lambda_{2p}^{-2}\lambda_{1b}^{-3}\left(\frac{Q}{\sqrt{\varepsilon\mu}L_1L_2}\right)^2 \sum_{n=1}^{N}\left(1+\frac{nd_0}{r\lambda_{1p}\lambda_{2p}}\right) &= \left(\lambda_{1b}-\lambda_{2p}^{-2}\lambda_{1b}^{-3}\right)\sum_{n=0}^{N+1}\left(1+\frac{nd_0}{r\lambda_{1p}\lambda_{2p}}\right) \\ &\quad + \frac{\alpha_k}{2}\left(\lambda_{1b}+\lambda_{1i}-2\lambda_{1p}/\lambda_s\right) + \alpha_B(\lambda_{1b}-\lambda_{1i}) \end{aligned}, \tag{21}$$

and

$$\frac{\Phi}{L_3}\sqrt{\frac{\varepsilon}{\mu}} = \lambda_{2p}^{-2}\lambda_{1b}^{-2}\left(\frac{Q}{\sqrt{\varepsilon\mu}L_1L_2}\right) \tag{22}$$

where $\alpha_B = B_0\lambda_s\lambda_{2p}/4\pi\mu r^3 d_0\lambda_{1p}$ is a dimensionless parameter related to the bending stiffness of the spring, and $Q/\sqrt{\varepsilon\mu}L_1L_2$ and $\Phi\sqrt{\varepsilon/\mu}/L_3$ are the dimensionless charge and dimensionless electrical load, respectively. Equations (21) and (22) are the state equations of the actuator in bending actuation and it can be verified that Equation (21) will reduce to Equation (16) when taking $Q = 0$, which means no electrical load is applied. The state curves of the actuator with different active layer numbers and different applied voltages are plotted in Figure 7. The solid line and the dash line represent the possible state under certain mechanical load (which is equal to 0 in Figure 7) and electrical load, respectively. The intersection of the solid line and the dash line gives the real state of the actuator under the given mechanical load and electrical load. Then the bending angle of the actuator could be calculated from Equation (6).

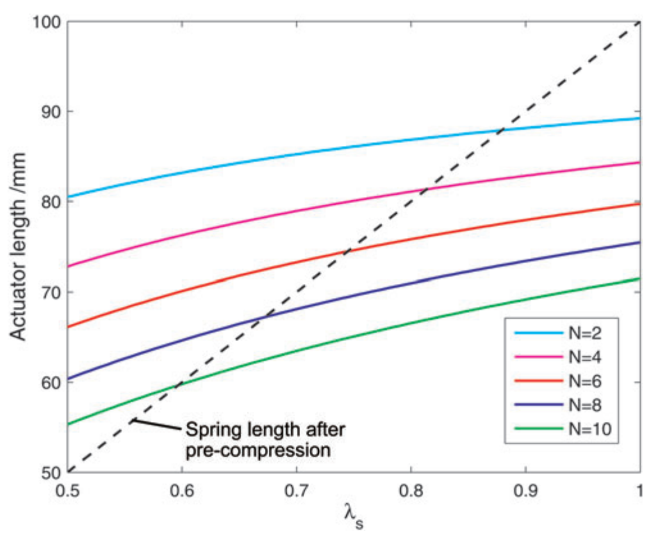

FIG. 6. The length of the actuators with different active layer numbers and different spring precompression ratios. Color images are available online.

Failure analysis

The failure of the spring-roll bending actuator is mainly due to the failure of the dielectric elastomers. In this article, we analyze the failure of the actuator considering some common failure modes of dielectric elastomers.

Electromechanical instability (EMI) is a common failure mode of dielectric elastomers. The thickness of the film will

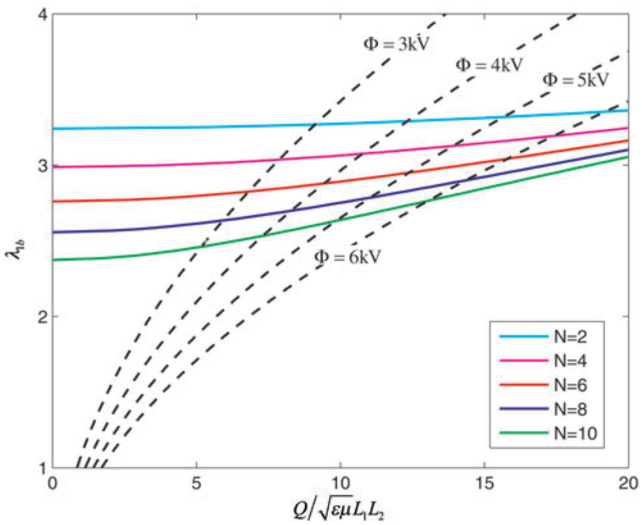

FIG. 7. State curves of the actuator under different electrical loads and without external mechanical load. Color images are available online.

decrease when the dielectric elastomer film is subjected to an external electric field. The decrease of the thickness will increase the electric field so that the thickness of the film will be further reduced. This positive feedback will drastically induce an electric field that is above the critical electric field so that failure occurs. To avoid such instability, the thermodynamic system should keep stable under some small perturbations. Thus, the Hessian matrix of the system should be positive definite.[38] Then we can get

$$\frac{\partial^2 H(\lambda_1, Q)}{\partial \lambda_1^2} > 0 \tag{23}$$

$$\frac{\partial^2 H(\lambda_1, Q)}{\partial Q^2} > 0 \tag{24}$$

$$\frac{\partial^2 H(\lambda_1, Q)}{\partial \lambda_1^2} \cdot \frac{\partial^2 H(\lambda_1, Q)}{\partial Q^2} > \left(\frac{\partial^2 H(\lambda_1, Q)}{\partial \lambda_1 \partial Q}\right)^2 \tag{25}$$

It is easy to verify that Equations (23) and (24) hold for any case. From Equation (25), we obtain the criterion for EMI as follows:

$$\begin{aligned}\lambda_{2p}^{-2}\lambda_{1b}^{-4}\left(\frac{Q}{\sqrt{\varepsilon\mu}\,L_1L_2}\right)^2 \sum_{n=1}^{N}\left(1+\frac{nd_0}{r\lambda_{1p}\lambda_{2p}}\right) = \\ \left(1+3\lambda_{2p}^{-2}\lambda_{1b}^{-4}\right)\sum_{n=0}^{N+1}\left(1+\frac{nd_0}{r\lambda_{1p}\lambda_{2p}}\right)+\alpha_B+\frac{\alpha_k}{2}.\end{aligned} \tag{26}$$

The actuator will fail due to EMI if the "=" is replaced by ">."

Electrical breakdown (EB) will occur when the electric field in the film is higher than the critical electric field E_c. Generally, E_c is not a constant and is dependent on the stretch ratio of the film. From the experimental data of Tröls *et al.*,[40] we take $E_c = 50V/\mu m$ as the critical electric field since the area stretch of the film in the actuator is close to that corresponding to this value. Since the material is assumed to be incompressible, we could have the electric field as $E = \Phi/\lambda_3 L_3 = \Phi\lambda_1\lambda_{2p}/L_3$. Then the criterion of the EB will be

$$E_c\lambda_{1b}\lambda_{2p}\sqrt{\frac{\varepsilon}{\mu}} = \frac{Q}{\sqrt{\varepsilon\mu}L_1L_2}. \tag{27}$$

When the applied voltage reached a critical value, the planar stress of the dielectric elastomer film may become zero. Further rise of the voltage will cause the film to wrinkle so that the actuator cannot work normally due to loss of tension. The critical conditions of loss of tension are $s_1 = 0$ and $s_2 = 0$. From the results of Moscardo *et al.*[36] and Zhao and Suo,[38] we could have

$$s_1 = 0: \quad \left(\frac{Q}{\sqrt{\varepsilon\mu}L_1L_2}\right)^2 = \lambda_{1b}^4\lambda_{2p}^2 - 1, \tag{28}$$

and

$$s_2 = 0: \quad \left(\frac{Q}{\sqrt{\varepsilon\mu}\,L_1L_2}\right)^2 = \lambda_{1b}^2\lambda_{2p}^4 - 1. \tag{29}$$

For dielectric elastomer film, when the stretch ratio is beyond the maximum value λ_m, with a representative value $\lambda_m = 5$, tensile rapture occurs. For the spring-roll actuator, the situation is a bit more complicated since the spring should be considered. When the arc length of the spring is equal to its free length, the spring cannot provide restoring force. It is also hard to make the spring elongate further by the actuation force of the dielectric elastomer. In this case, we could have $\lambda_{1b}L_1 = L_0$ or $\lambda_{1b} = \lambda_{1p}/\lambda_s$. Then the actuator will fail when the longitudinal stretch ratio reaches the critical value, namely

$$\lambda_{1b} = \lambda_c, \tag{30}$$

where $\lambda_c = \min(\lambda_m, \lambda_{1p}/\lambda_s)$. In fact, there is another case that the spring is in solid length, which means the spring

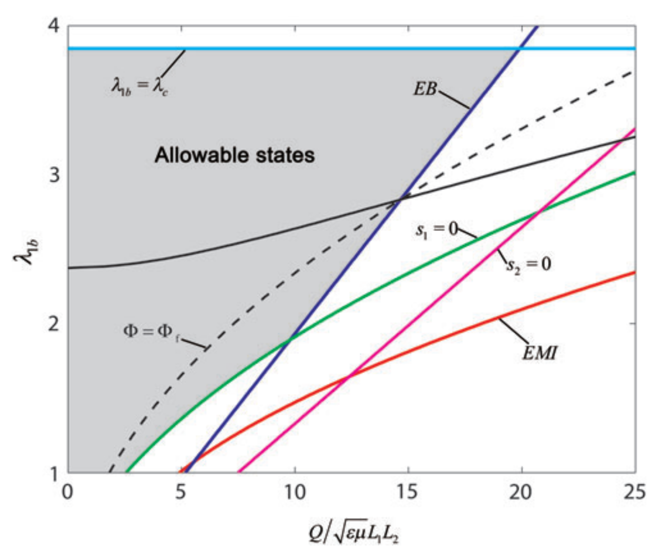

FIG. 8. The allowable states of the actuator constrained by the curves that represent different failure modes. Color images are available online.

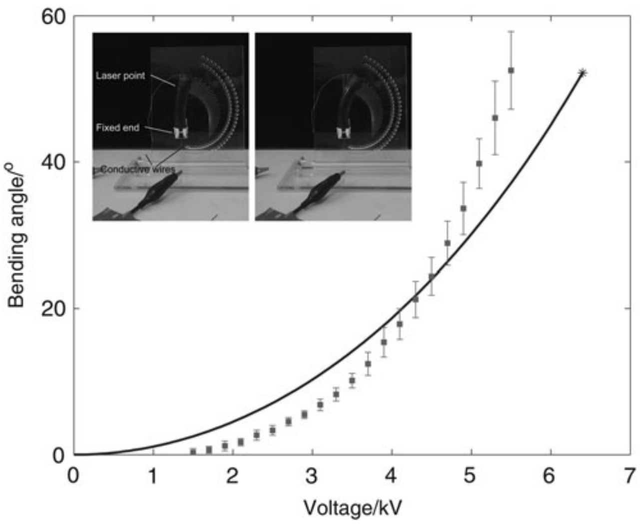

FIG. 9. Comparison between the theoretically predicted and tested bending angle/voltage relationships with the inset picture showing the setup used for bending angle measurement.

coils contact each other. Because the dielectric elastomer film will stretch in a longitudinal direction subjected to external electric field, this case only occurs after fabrication and is not discussed as a failure mode here. Too much compression will lead to plasticity of the spring and thus the actuator may not work normally if the actuator length is less than half of the free length of the spring. The actuator length could be calculated using the methods in initial deformation analysis.

After getting all the criteria of some failure mode, we could analyze the allowable states of the actuator. All the curves that represent above failure modes are plotted in Figure 8. The gray area in Figure 8 represents the region of allowable states, inside which the actuator could work safely without failure. The dark line represents all the possible states of the actuator with no external mechanical load from Equation (21) and the intersection of the dark line and the color line means that the actuator will fail in the corresponding failure mode. Among all the intersections, the one with the least stretch ratio is defined as the failure state, and the failure voltage Φ_f could be calculated combining Equation (22).

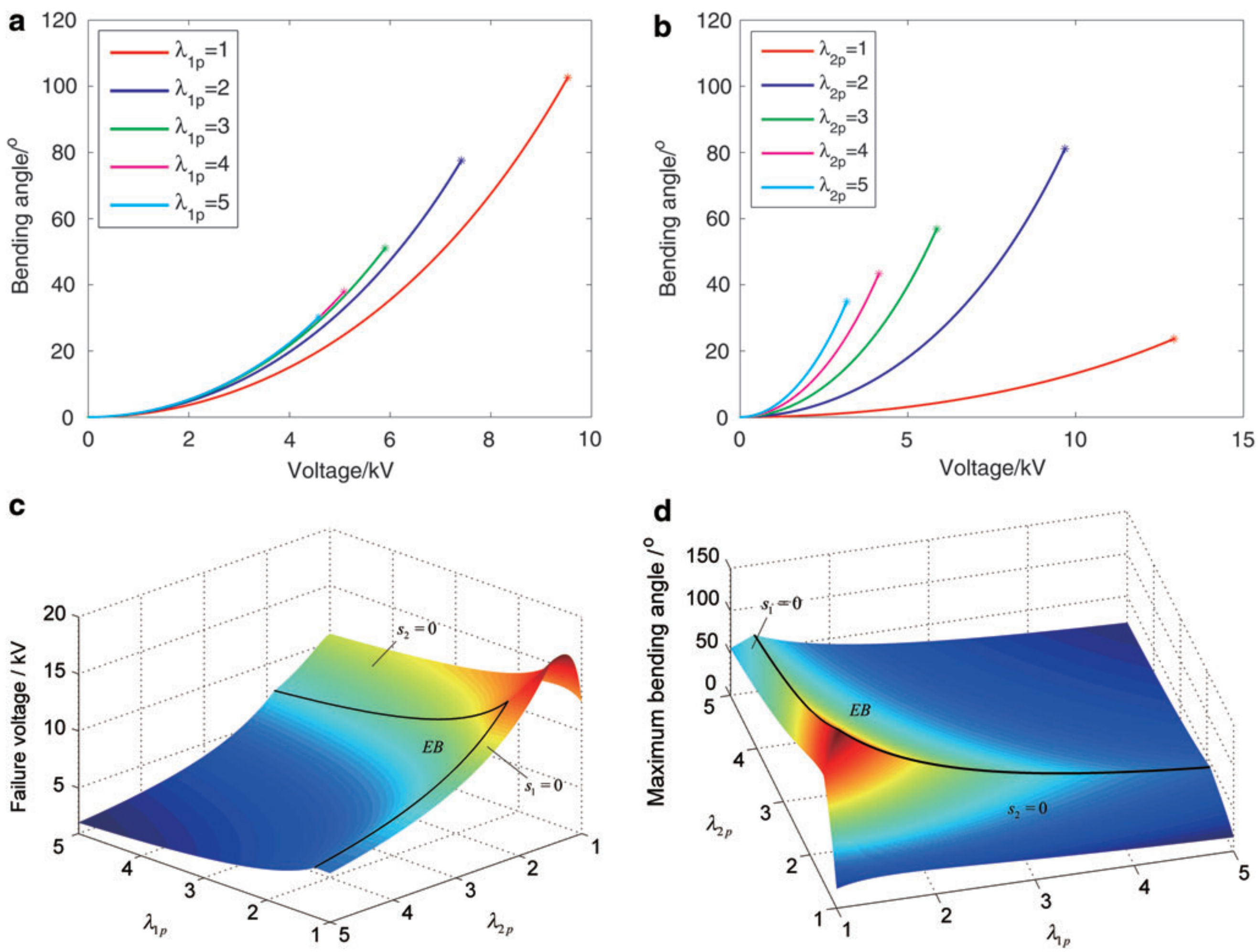

FIG. 10. The performances of the actuators with different **(a)** longitudinal prestretch ratios and **(b)** circumferential prestretch ratios. The **(c)** failure voltages and **(d)** maximum bending angles of the actuators with different longitudinal and circumferential prestretch ratios. The *black lines* in **(c)** and **(d)** show the critical conditions to avoid loss of tension. Color images are available online.

Actuator Design

Using the above model, we could conduct some parameter designs of the dielectric elastomer spring-roll bending actuator. Before that, the theoretical predictions and test results of the performance of the actuator are compared to verify this model. The setup for bending angle test is shown in the inset picture of Figure 9. One end of the actuator is fixed and the laser displacement sensor (LK-G3000 series from KEYENCE Corporation) is used to measure the deflection of the actuator. The applied voltage is generated from the DC power supply and amplified by the high-voltage amplifier (Trek Model 10/40A). To improve the accuracy of the results, when the applied voltage is low, the laser point is set on the top end of the actuator and then near the middle when the voltage is high enough. The distance between the laser point and the fixed end is recorded so that the bending angle could be calculated from the geometrical relationships.

The parameters of the tested actuators are the same as that listed in Table 1. The theoretical calculations and the test data are plotted in Figure 9. The point marked in ''*'' represents the theoretical failure point. It should be noted that the tested failure voltage of the actuator is discrete due to some possible defects inside the VHB film or induced when fabrication, and the minimum value of the tested actuators is 5.5 kV.

By comparison, our model cannot give a very accurate fit of the test curve due to some idealizations and simplifications when modeling this complex system. One of the reasons for such an imprecise fit is that the neo-Hookean model could not well describe the mechanical behavior of the dielectric elastomers under large deformation. Supplementary Figure S1 shows the comparison between the uniaxial tensile test data (Zwick Z010 with 1 kN load cell) and the fitted data using a neo-Hookean model. The area strain of the VHB film after prestretch in the bending actuator is higher than 6. However, the difference between the test data and fitted data becomes larger when the strain is larger than 8, which corresponds to an area strain of about 2.8 for the incompressible materials. However, this model could still be effective and convenient in predicting the trend of the bending angle as the applied voltage rises and in analyzing the influence of each parameter on the performance of the actuator.

In the following parts, we discuss the design and optimization of the actuator concerned with the design parameters

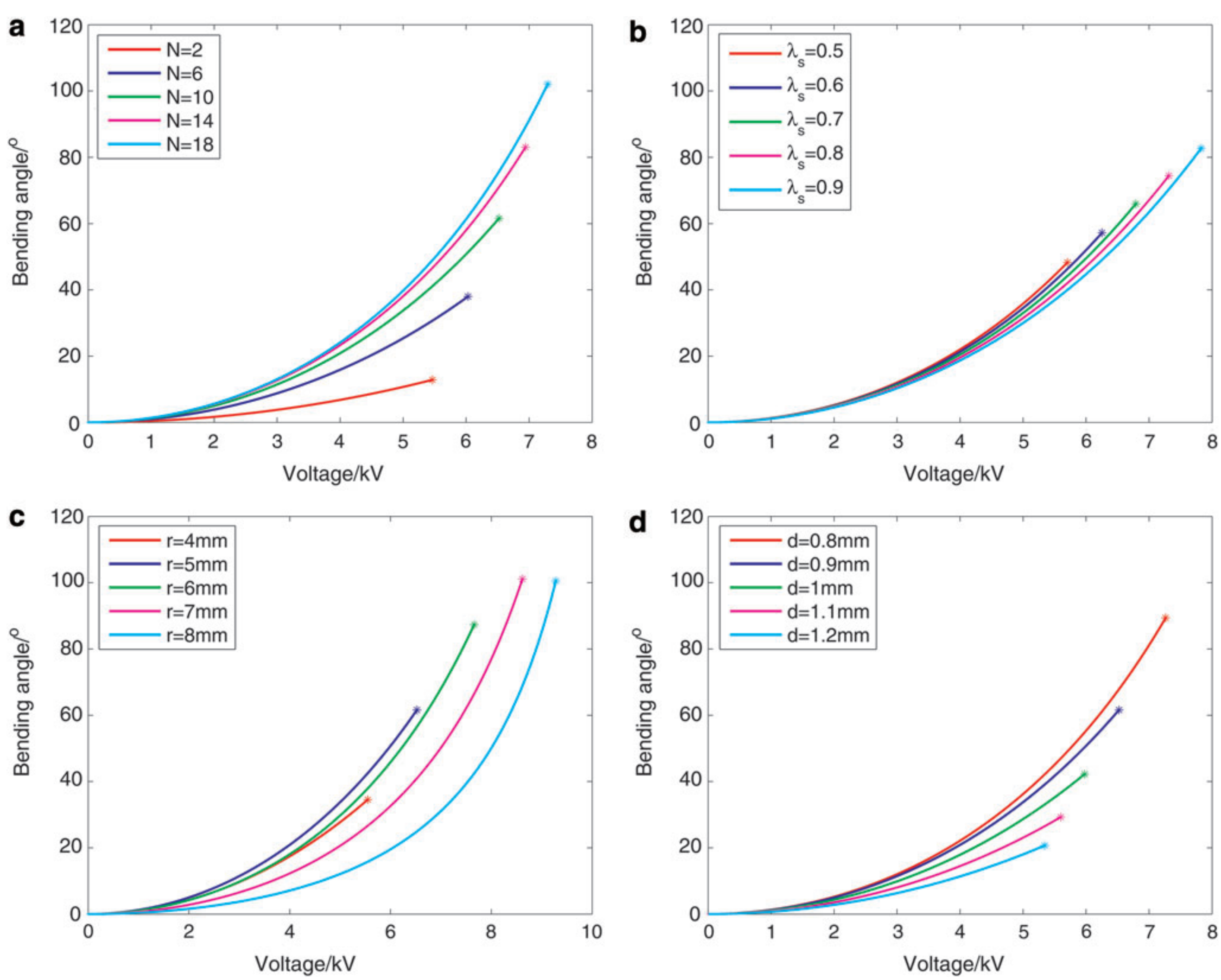

FIG. 11. The performances of the actuators with different **(a)** layer numbers, **(b)** spring precompression ratios, **(c)** outside radii of spring, and **(d)** spring wire diameters. Color images are available online.

listed in Table 1. Generally, the optimization goal is to achieve a large bending angle of the actuator at a relatively low applied voltage. Besides, there could be some other cases based on different conditions and requirements. The bending angle/voltage curves, maximum bending angles, and failure voltages of the actuators with different design parameters could be plotted. It should be noted that in the following part the values of parameters except for the concerned parameter are fixed and chosen from Table 1.

The performances of the actuators with different longitudinal prestretch ratio λ_{1p} and circumferential prestretch ratio λ_{2p} are plotted in Figure 10a and b. Figure 10c and d, respectively, gives the failure voltages and maximum bending angles of the actuators with different λ_{1p} and λ_{2p}. As can be seen from the figures, when the prestretch ratio is small, the failure mode is loss of tension and a relatively high voltage will be required to achieve the same bending angle. The dark line in Figure 10c, d represents the critical conditions between failure modes of loss of tension and EB. A minimum prestretch ratio of 1.3×1.9 will be required to avoid loss of tension and also reduce the actuation voltage.

The influence of the longitudinal prestretch ratio on the shape of the bending angle/voltage curve is slighter than that of the circumferential prestretch ratio. That is because the restore force of the spring could reduce the differences in the longitudinal prestretch ratio after the system is in equilibrium. However, such differences could not be fully eliminated, so the failure voltage and maximum bending angle will decrease with the increasing of λ_{1p} when the failure mode is EB. The circumferential prestretch ratio mainly determines the thickness of the VHB film. The larger the λ_{2p} is, the thinner the film will be. When λ_{2p} is large enough to avoid loss of tension, larger λ_{2p} could give a large bending angle and also lower failure voltage. Based on the above two factors, the maximum bending angle will decrease with the increasing of λ_{2p}, but at a speed lower than that when λ_{1p} changes.

The active layer number N also has certain influences on the performance of the actuator. As discussed above, when N is small, the VHB film will be further stretched by the spring, leading to smaller film thickness and longer actuator length. That will reduce the deformability of the actuator and also the failure voltage (Figs. 11a and 12a). Principally, large active layer numbers would be good. However, the spring may be in plastic deformation at a large N. A layer number that could make the actuator length half of the free length of the spring would be suitable.

The influence of precompression ratio λ_s on the performances of the actuator is shown in Figures 11b and 12b. λ_s could determine the initial longitudinal stretch ratio and the axial restoring force. Similar to λ_{1p}, the shapes of the bending

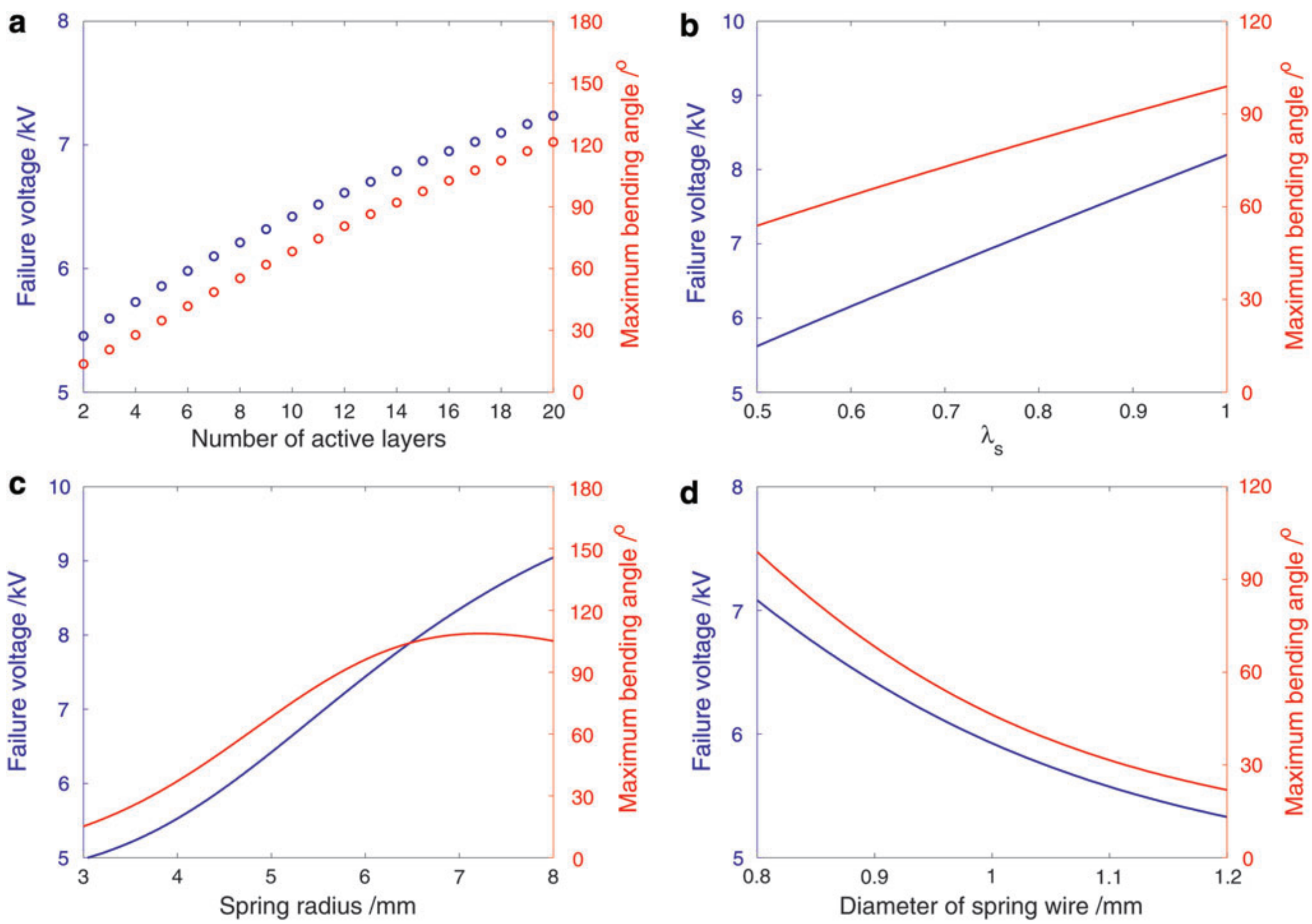

FIG. 12. The failure voltages and maximum bending angle of the actuators with **(a)** layer numbers, **(b)** spring precompression ratios, **(c)** outside radii of spring, and **(d)** spring wire diameters. Color images are available online.

angle/voltage curves when λ_s changes are very close and the failure voltage of the actuator increases since large λ_s will lead to thicker film. Moreover, the influence of λ_s on the failure voltage and maximum bending angle is nearly linear (Fig. 12b), making it possible to finely tune the actuator performance.

Both the outside radius r and the wire diameter d can determine the stiffness of the spring. Since d has higher order than r in the expressions of k and B_0, the wire diameter is a vital parameter that can severely influence the actuator performance. Generally, larger d could make the spring stiffer and thus decrease the deformability of the actuator dramatically and also the failure voltage (Figs. 11d and 12d). For the outside radius r, the case is complex since r is also a geometry-related parameter that shows influence on the bending angle of the actuator (Eq. (6)). When r increases, the actuator could have larger deformation and failure voltage since the spring stiffness decreases, while the bending angle would decrease mathematically. That makes the relationship between the bending angle and outside radius of spring not monotonic (Figs. 11c and 12c) so that an optimal value of the outside radius could be obtained.

When the length of the spring increases, we can simply regard it as several actuator elements that are connected in parallel if other parameters remain invariable, which coincides with the predicted results. Ideally, the failure voltage will not change and the bending angle will increase linearly with the increasing of the spring length, as shown in Supplementary Figure S2. In fact, as mentioned before, buckling will occur when the spring is too long. In this circumstance, some assumptions in our model will not be valid.

Discussions and Conclusions

In this article, we fabricated the dielectric elastomer spring-roll actuators with large electrically induced bending angle. A three-finger flexible gripper consisting of 3D-printed structures and three actuators was fabricated and demonstrated the grasping and releasing operations incorporated with a remotely controlled toy crane truck. The pull-out force of the gripper is measured to be 228.3 mN when the applied voltage is 5 kV. We have also made an inchworm-inspired crawling robot that could move forward under alternating voltages. The oriented fibers are used to provide anisotropic friction to improve the performance of the crawling robot. Under the external sinusoidal voltage with amplitude of 0–6 kV and frequency of 20 Hz, the speed of the crawling robot could reach at 26.3 mm/s.

We also established a thermodynamic model of the spring-roll actuator to investigate the initial deformation and bending deformation. The failure of the actuator has been analyzed considering some common failure modes, including EMI, EB, loss of tension, and critical stretch ratio. To verify the suitability of this model, we built a setup to use laser to measure the bending angle/voltage relationships of the actuator as a reference to theoretical prediction. The influence of some design parameters on the performance of the actuator is discussed in detail. The EMI of the actuator could be avoided since the resilience force of the spring could keep the prestretch state of the dielectric elastomer film.[38] If the dielectric elastomer film is not prestretched or the prestretch ratio is too low, the failure mode will be loss of tension and a higher actuation voltage will be required. With the parameters used in this article, a minimum biaxial prestretch ratio of 1.3×1.9 is suggested to avoid loss of tension. The precompression ratio of the spring seems to be a parameter that could finely tune the properties of the actuator, and the outside radius of the spring could be optimized due to its complicated influence on the performance of the actuator. These results will be helpful in the design and optimization of the spring-roll bending actuators.

In future work, we hope to find more applications of the dielectric elastomer spring-roll actuator and optimize the parameters of the actuator based on different scenarios using the results in this article. We would also like to improve the model of the actuator to predict the performance of the actuator more accurately.

Acknowledgments

This work is supported by the National Natural Science Foundation of China (grant no. 11632005 and 11772109).

Author Disclosure Statement

No competing financial interests exit.

References

1. Lipson H. Challenges and opportunities for design, simulation, and fabrication of soft robots. Soft Robot 2014;1:21–27.
2. Kim S, Laschi C, Trimmer B. Soft robotics: a bioinspired evolution in robotics. Trends Biotechnol 2013;31:287–294.
3. Laschi C, Mazzolai B, Cianchetti M. Soft robotics: technologies and systems pushing the boundaries of robot abilities. Sci Robot 2016;1:eaah3690.
4. Ilievski F, Mazzeo AD, Shepherd RF, *et al.* Soft robotics for chemists. Angew Chem 2011;123:1930–1935.
5. Shepherd RF, Ilievski F, Choi W, *et al.* Multigait soft robot. Proc Natl Acad Sci 2011;108:20400–20403.
6. Tolley MT, Shepherd RF, Mosadegh B, *et al.* A resilient, untethered soft robot. Soft Robot 2014;1:213–223.
7. Shepherd RF, Stokes AA, Freake J, *et al.* Using explosions to power a soft robot. Angew Chem 2013;125:2964–2968.
8. Martinez RV, Branch JL, Fish CR, *et al.* Robotic tentacles with three-dimensional mobility based on flexible elastomers. Adv Mater 2013;25:205–212.
9. Hawkes EW, Blumenschein LH, Greer JD, *et al.* A soft robot that navigates its environment through growth. Sci Robot 2017;2:eaan3028.
10. Seok S, Onal CD, Cho KJ, *et al.* Meshworm: a peristaltic soft robot with antagonistic nickel titanium coil actuators. IEEE/ASME Trans Mechatron 2013;18:1485–1497.
11. Lin HT, Leisk GG, Trimmer B. GoQBot: a caterpillar-inspired soft-bodied rolling robot. Bioinspiration Biomimetics 2011;6:026007.
12. Laschi C, Cianchetti M, Mazzolai B, *et al.* Soft robot arm inspired by the octopus. Adv Robot 2012;26:709–727.
13. Sugiyama Y, Hirai S. Crawling and jumping by a deformable robot. Int J Robot Res 2006;25:603–620.
14. Peng Q, Wei H, Qin Y, *et al.* Shape-memory polymer nanocomposites with a 3D conductive network for bidirectional actuation and locomotion application. Nanoscale 2016;8: 18042–18049.

15. Pei Q, Rosenthal M, Stanford S, *et al.* Multiple-degrees-of-freedom electroelastomer roll actuators. Smart Mater Struct 2004;13:N86–N92.
16. Pelrine R, Kornbluh R, Pei Q, *et al.* Dielectric elastomer artificial muscle actuators: toward biomimetic motion. Proc SPIE 2002;4695:126–137.
17. Pei Q, Rosenthal MA, Pelrine R, *et al.* Multifunctional electroelastomer roll actuators and their application for biomimetic walking robots. Proc SPIE 2003;5051:281–290.
18. Shian S, Bertoldi K, Clarke DR. Dielectric elastomer based ‘‘grippers’’ for soft robotics. Adv Mater 2015;27:6814–6819.
19. Shintake J, Rosset S, Schubert B, *et al.* Versatile soft grippers with intrinsic electroadhesion based on multifunctional polymer actuators. Adv Mater 2016;28:231–238.
20. Shen Q, Wang T, Liang J, *et al.* Hydrodynamic performance of a biomimetic robotic swimmer actuated by ionic polymer–metal composite. Smart Mater Struct 2013;22:075035.
21. Chen Z, Um TI, Bart-Smith H. A novel fabrication of ionic polymer–metal composite membrane actuator capable of 3-dimensional kinematic motions. Sens Actuators A Phys 2011;168:131–139.
22. Firouzeh A, Ozmaeian M, Alasty A. An IPMC-made deformable-ring-like robot. Smart Mater Struct 2012;21:065011.
23. Zhang J, Yao Y, Sheng L, *et al.* Self-fueled biomimetic liquid metal mollusk. Adv Mater 2015;27:2648–2655.
24. Shepherd RF, Stokes AA, Nunes R, *et al.* Soft machines that are resistant to puncture and that self seal. Adv Mater 2013;25:6709–6713.
25. Sadeghi A, Tonazzini A, Popova L, *et al.* Robotic mechanism for soil penetration inspired by plant root. In: 2013 IEEE International Conference on Robotics and Automation (ICRA). Karlsruhe, Germany; IEEE: 2013;3457–3462.
26. Pelrine R, Kornbluh R, Pei Q, *et al.* High-speed electrically actuated elastomers with strain greater than 100%. Science 2000;287:836–839.
27. Brochu P, Pei Q. Advances in dielectric elastomers for actuators and artificial muscles. Macromol Rapid Commun 2010;31:10–36.
28. Kovacs G, Lochmatter P, Wissler M. An arm wrestling robot driven by dielectric elastomer actuators. Smart Mater Struct 2007;16:S306–S317.
29. Carpi F, De Rossi D. Bioinspired actuation of the eyeballs of an android robotic face: concept and preliminary investigations. Bioinspiration Biomimetics 2007;2:S50–S63.
30. Carpi F, Frediani G, Turco S, *et al.* Bioinspired tunable lens with muscle-like electroactive elastomers. Adv Funct Mater 2011;21:4152–4158.
31. Kofod G, Wirges W, Paajanen M, *et al.* Energy minimization for self-organized structure formation and actuation. Appl Phys Lett 2007;90:081916.
32. Jordi C, Michel S, Fink E. Fish-like propulsion of an airship with planar membrane dielectric elastomer actuators. Bioinspiration Biomimetics 2010;5:026007.
33. Lochmatter P, Kovacs G. Design and characterization of an active hinge segment based on soft dielectric EAPs. Sens Actuators A Phys 2008;141:577–587.
34. Kollosche M, Zhu J, Suo Z, *et al.* Complex interplay of nonlinear processes in dielectric elastomers. Phys Rev E 2012;85:051801.
35. Suo Z. Theory of dielectric elastomers. Acta Mech Solida Sin 2010;23:549–578.
36. Moscardo M, Zhao X, Suo Z, *et al.* On designing dielectric elastomer actuators. J Appl Phys 2008;104:093503.
37. Zhu J, Stoyanov H, Kofod G, *et al.* Large deformation and electromechanical instability of a dielectric elastomer tube actuator. J Appl Phys 2010;108:074113.
38. Zhao X, Suo Z. Method to analyze electromechanical stability of dielectric elastomers. Appl Phys Lett 2007;91:061921.
39. Zhang YH, Liu HH, Wang DC (Eds). Spring Handbook (Second Edition, in Chinese). Beijing: China Machine Press, 2008.
40. Tröls A, Kogler A, Baumgartner R, *et al.* Stretch dependence of the electrical breakdown strength and dielectric constant of dielectric elastomers. Smart Mater Struct 2013;22:104012.

Address correspondence to:
Jinsong Leng
Center for Composite Materials and Structures
Harbin Institute of Technology
2 YiKuang Street
Harbin 150080
China

E-mail: lengjs@hit.edu.cn